Simulation of flow around a slender body at high angles of attack

Osama Obeid[1,a] and Ibraheem Alqadi[1]

[1]*Aeronautical Engineering Department, King Abdulaziz University, Jeddah, Saudi Arabia*

Abstract. LES of the flow around an ogive-cylinder body at high angles of attack were carried out to investigate the possibility of the development of asymmetric wake-vortex without the introduction of artificial perturbations. The study investigated the effect of grid resolution and scheme bias on the solution. The numerical solution was found to be sensitive to the bias in the numerical scheme. The simulation was carried for angles of attack $\alpha = 30°$, $40°$, $50°$, $55°$, and $60°$. The simulation at $\alpha = 30° - 40°$ produced symmetric wake-vortex. At $\alpha = 50°$, the wake-vortex is also symmetric but with vortex separation. At $\alpha = 55°$, the wake-vortex becomes asymmetric. At α =60°, the wake-vortex is highly asymmetric with vortex separation and breakdown. It was concluded that asymmetric flow around slender bodies at high angles of attack can be simulated in the absence geometrical or flow perturbations.

1 Introduction

When slender bodies fly at high angles of attack, a wake-vortex system is generated on the leeward side. At small angles, the wake-vortex is symmetric and attached to the body. However, as the angle of attack is increased, the wake-vortex becomes asymmetric. As a result, side force is generated. This presents control difficulties. The lack of understanding of this phenomenon is due to the difficulties encountered when performing either experimental or numerical studies. The obstacles in experimental studies include model imperfections, incoming flow conditions, and limitations of available measurements techniques. On the other hand, high fidelity numerical studies are demanding. DNS for such flows is not feasible given the flow resolution requirements. Large Eddy Simulation (LES) provides an alternative to DNS. In LES, the Navier-Stokes equations are solved to resolve large-scale turbulent structures while modelling the effects of small-scale structures. Most of previous numerical studies were performed using RaNS and/or URaNS in which the introduction of artificial perturbations [1,2], or geometrical imperfections [3], is necessary to generate flow asymmetry. Likewise, some of the available LES studies [4] had to add artificial perturbations as well whereas others argue that asymmetry can be captured without them. On the other hand, experimental studies are limited by the resolution and accuracy of available measurement techniques. Experimental measurement, conducted by Zilliac, Degani, and Tobak [5], showed four different flow pattern; symmetric flow on the leeward side for ($\alpha < 30^\circ$), steady asymmetry flow within the range of ($30^\circ > \alpha > 50^\circ$), nearly bi-stable range ($50^\circ > \alpha > 65^\circ$), and bluff body vortex shedding for

[a] Corresponding author: oobeid@stu.kau.edu.sa

($\alpha > 65^{\circ}$). In addition, a peculiar behaviour is observed where the side force direction changes with model revolution [5,6]. Further experimental studies revealed a number of factors that influence this asymmetry such as Mach number [7,8], Reynolds number [7], nose bluntness, and fineness ratio [8].

From a numerical point of view, the separated, unsteady, asymmetric flow around a slender body at high angle of attack poses several challenges. The main complexity arises from the unsteady viscous flow behind the wake-vortex where nonlinearity effects are dominant. Also, the behaviour of the wake-vortex is complex where the flow exhibits vortex interaction, separation, and breakdown. With such complexity, a simulation would require resolving flow behaviour. Degani and Schiff [1], Murman [2], and Degani et al [9] performed computational studies using Thin-Layer RaNS. However, the simulations showed that flow asymmetry did not develop in the absence of geometrical or flow perturbations. The objective of this study is to investigate the development of asymmetric wake-vortex around slender bodies at high angle of attack using Large Eddy Simulation without the introduction of neither geometrical nor flow perturbations. A grid-refinement study was performed to investigate the sensitivity of the solution to grid resolution and numerical scheme. The study was carried out for at angle of attack $\alpha = 30^{\circ}$ and 60°. Statistical analysis was performed to investigate time averaged solution. In addition, mean normal and side force coefficients (C_y, C_z) were computed and analysed.

2 Computational Setup

Calculations were carried out using Large-Eddy-Simulation approach in which three-dimensional time-dependent Navier-Stokes and continuity equations are solved numerically after being spatially filtered for all motions with a scale larger than the mesh size of the chosen numerical grid. The small-scale, mainly dissipative motion, is simulated by a sub-grid scale (SGS) model. The filtered equations read in tensor notation:

$$\frac{\partial \overline{u}_i}{\partial x_i} = 0 \tag{1}$$

$$\frac{\partial \overline{u}_i}{\partial t} + \frac{\partial \overline{u}_i \overline{u}_j}{\partial x_j} = -\frac{1}{\rho}\frac{\partial \overline{p}}{\partial x_i} + \frac{\partial \left(2\nu \overline{S}_{ij}\right)}{\partial x_j} - \frac{\partial \tau_{ij}}{\partial x_j} \tag{2}$$

The equations are written in compact index-notation. i and j varies from 1 to 3. $\overline{u}_i$ represents velocity vector components and $\overline{p}$ is pressure. The fluid density is ρ and the kinematic molecular viscosity is ν. The spatially filtered quantities are denoted with overbar. The last term in Navier-Stokes equation is the gradients of the sub-grid-scale stresses $\tau_{ij} = \overline{u_i u_j} - \overline{u}_i \overline{u}_j$ that is modelled using the eddy-viscosity concept:

$$\tau_{ij} = 2\nu_t \overline{S}_{ij} + \frac{1}{3}\delta_{ij}\tau_{kk} \quad , \quad \overline{S}_{ij} = \frac{1}{2}\left(\frac{\partial \overline{u}_i}{\partial x_j} + \frac{\partial \overline{u}_j}{\partial x_i}\right) \tag{3}$$

For larger scale motions, spatial filtering is used on the three-dimensional time-dependent Navier-Stokes equations before being solved numerically. Dynamic Smagorinsky model, developed by Germano et al [10] and enhanced by Lilly [11], will be used to compute the eddy viscosity of the sub-grid scale.

$$\nu_t = C_S \Delta^2 \left|\overline{S}\right| \text{ Where } \overline{S} = (2\overline{S}_{ij}\overline{S}_{ij})^{\frac{1}{2}} \text{ and } \Delta = \left(\Delta x \Delta y \Delta z\right)^{\frac{1}{3}} \tag{4}$$

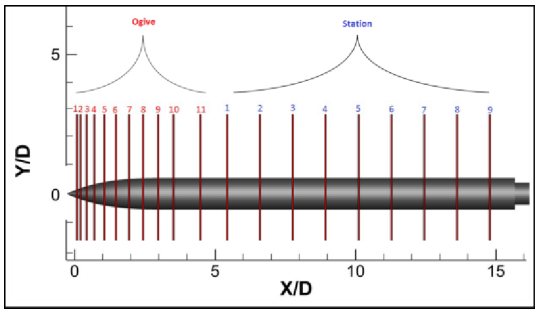

Figure 1: Stations.

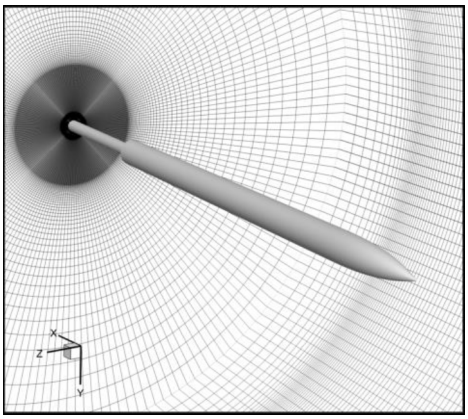

Figure 2: Computational Grid

The coefficient C_s is computed with the Dynamic Smagorinsky-Lilly procedure where a second filter is implemented with twice the width Δ based on the grid spacing. The difference between the two filtered solutions is used to compute C_s dynamically. For a physical solution, the value of C_s is limited to ($0.0 < C_s < 0.23$). The geometry used in the study is identical to the model used by [12] which consisted of fineness ratio of 3.5 and 12.5 for tangent ogive and cylindrical afterbody, respectively. A model holder was added at the end of the cylinder with a length of 11.5D and a diameter of 0.5D. The overall length of the model is about 34.5cm and the diameter is D = 2.16cm for the cylindrical afterbody. The time history of the solution is collected at 11 stations along the Ogive and 9 stations along the cylinder (figure 1). The Ogive profile matching the one used in the experiment model is computed as $y = D/\ (1-(1-x/L))^{2.75}$. L is set equal to $3.544D$. The length of the ogive (L) is taken slightly more than $3.5D$ in order to compensate the loss in length after adding a small hemisphere to simulate the nose. Since it is not possible from a practical point of view to manufacture a perfectly sharp tip. Hence, a hemisphere will be added at the nose with a radius of $0.025D$, where D = 2.16cm. The computational domain is setup such that the domain boundaries are $6.5D$ upstream of the nose, $11.5D$ downstream of the cylinder base, and $15D$ in the radial direction away from the model. The base computational grid consisted of 8.7 million hexahedral cells distributed as follows: 220 in the longitudinal direction, 194 in the radial direction, and 197 in the azimuthal direction (figure 2). The initial base grid spacing in the radial direction (r), the steam-wise direction (x), and the azimuthal direction (θ) are $\Delta r^+ = 10$, $\Delta x^+ = 9$, and $\Delta\theta^+ = 80$ wall units. It should be noted that the above estimated wall spacing is for attached turbulent boundary layer. However, the separation in this case is laminar and transition to turbulence takes place in the separated shear layer. The computations were carried out using Ansys-Fluent V17.0. The pressure-based solver uses SIMPLE scheme for pressure-velocity coupling, the Least Square approach for gradients evaluation, and 2nd order pressure interpolation scheme. The solution is advanced in time using implicit 2nd order time marching scheme. For spatial discretization, two spatial discretization schemes were used to assess the effect of scheme bias on the solution; 2nd order Central scheme and 2nd order Bounded Central scheme.

Table 1. Grid size (in millions) for each grid refinement level.

	1: Δx	**2**: $\Delta x / 2$	**3**: $\Delta x / 4$
A: $\Delta\theta$	8.70	13.87	24.21
B: $\Delta\theta / 2$	11.26	17.88	31.16
C: $\Delta\theta / 4$	19.25	34.43	52.88

3 Results and Discussion

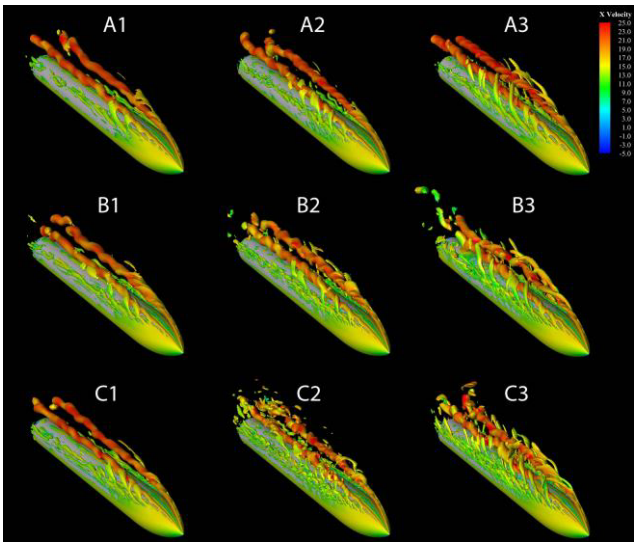

Figure 3. λ-2 criterion (Bounded)

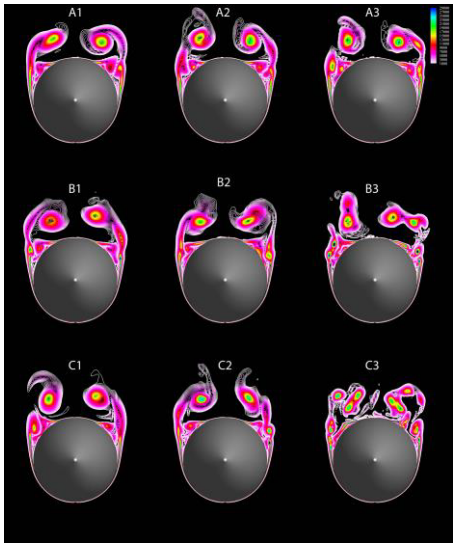

Figure 4. Instantaneous *x*-vorticity (Bounded)

The Time step was set to 10^{-4} seconds with a maximum of 20 error-reduction sub-iterations per time-step and a maximum residual of 10^{-5}. Extrapolation was used at the out-flow boundary while velocity components were specified at the inflow boundary. The density and viscosity are held constant at 1.225 kg. m^{-3} and 1.784× 10^{-5} kg. $(m. s)^{-1}$, respectively. The freestream velocity is set such that the Reynolds number, based on model diameter D = 2.16 cm, is $\mathrm{Re}_D = 26{,}000$. Two levels of grid refinement were performed in both the azimuthal and the axial directions as shown in Table 1. For the grid refinement study, calculations were performed at $\alpha = 30°$. The solutions were advanced 18 flow-through times (7000 time steps) to allow for flow field development. Flow statistics is then collected over 14000 time steps. Additionally, instantaneous data of the solution at 20 stations along the model, shown in figure 1, were also saved.

Figure 3 shows instantaneous iso-surfaces of λ-2 criterion for the grid configurations listed in Table 2. The figure illustrates the increase in the number of captured flow scales with grid refinement. Contour plots of the instantaneous x-vorticity on the *y-z* plane at Ogive-11 are depicted in figure 4 for Bounded Central scheme. In case A1, the wake-vortex system is captured as two large vortices. As the grid is refined, the captured wake-vortex system consists of several smaller vortical structures. It is noted that the refinement in the axial direction (cases A1, A2, and A3) has a stronger effect on the solution compared with the effect of refinement in the azimuthal direction (cases A1, B1, and C1). However, the combined effect of refinement in both directions (case C3) produces higher resolution of the wake-vortex system. Table 2 shows a comparison of the solution using Bounded Central scheme with the standard central scheme. There is a noticeable difference between the two spatial schemes as the grid is refined, especially in case C3. The Bounded Central scheme demonstrate multiple small vortical structures for case C3 whereas the Central scheme shows the primary wake-vortex accompanied with unsteady small structures.

Figure 5 depicts the normal and side force coefficients of all investigated grids along the model stations. For the first 6 station, up to Ogive-6, the side and normal forces are virtually identical for all cases. Starting form Ogive-1, the normal force coefficient (C_y) grows reaching a maximum at Ogive-6. Downstream of Ogive-6, C_y starts to decrease but with disparity between the different cases. Oscillations in the force coefficient appear distinctively for the Bounded Central scheme. However, the oscillation diminishes with grid refinement. This applies to refinements from "1" to "2" in axial direction. Further refinement,"3", increases the fluctuation. Similarly, the side force coefficient, C_z, decreases as the grid is refined in the azimuthal direction, "A" to "B", for Bounded Central scheme. Additional refinement in the azimuthal direction, "B" to "C", or in the longitudinal direction, "1" to

"2" and "2" to "3", increases the side force coefficient downstream Ogive 9. In general, the side force increases for all grids downstream Ogive 9. Also, the direction of side force varies with respect to grid size. Cases A1, A2, B2, and B3 exhibit negative C_z whereas A3, B1, C1, C2, C3 have a positive C_z.

Table 2. Comparison of instantaneous *x*-vorticity.

	A1	B2	C3
Bounded Central scheme	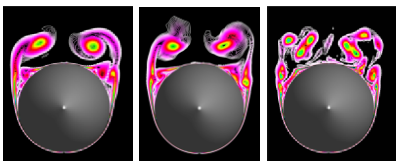		
Central scheme	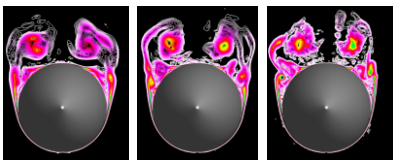		

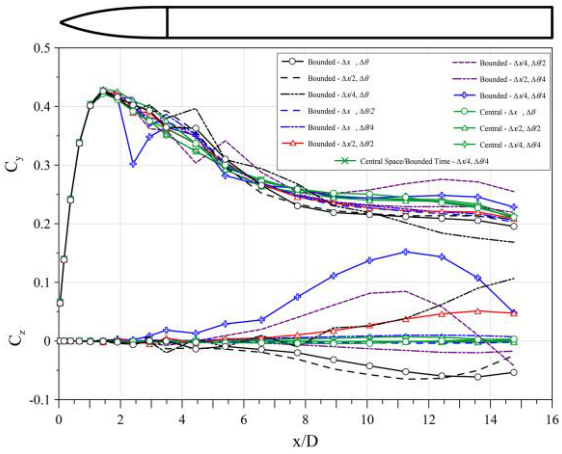

Figure 5. Variation of normal and side forces with grid resolution and spatial scheme

The maximum side force coefficient was obtained close to Station 6 for case C3 with a magnitude of $C_z = 0.152$ (62% of C_y). Moreover, using the Central scheme shows marginal variation in normal and side force coefficients with respect to grid refinement, cases A1, B2, and C3. The direction of the side force coefficient changes slightly as the grid is refined. For case A1 using Central scheme, the side force coefficient was negative downstream Ogive 9. B2 refinement decreased the magnitude of side force coefficient. As the grid is refined further, C3, the side force coefficient slightly increases to become positive. The maximum side force coefficient for the Central scheme was obtained at Station 6 for C3 grid with a magnitude of $C_z = 0.00715$ which is 2.9% of C_y at that location. While the Central scheme produced almost zero side force, symmetric wake-vortex, the Bounded central scheme produced considerable side force, asymmetric wake-vortex. Additionally, the Central scheme produces consistent solution behaviour with grid refinements, while the Bounded Central scheme exhibit large and inconsistent behaviour with grid refinement. The difference in scheme behaviour can be attributed to the bias built in the Bounded scheme. Figure 6 displays instantaneous iso-surfaces of λ-2 criterion and stream traces emitted from the nose at $\alpha = 40°$, $50°$, $55°$, and $60°$ using the Central scheme. The solution produced symmetric and attached wake-vortex at $\alpha = 40°$. At $\alpha = 50°$, the wake-vortex is also symmetric but with vortex separation. At $\alpha = 55°$, the asymmetry started to develop along the cylinder with asymmetric vortex separation. However, the wake-vortex at $\alpha = 60°$ is highly asymmetric with vortex separation starting near the nose with subsequent vortex breakdown further downstream. The results illustrate, numerically, the development of asymmetric wake-vortex in the absence of geometrical imperfections or flow perturbations.

4 Conclusion

LES of the flow around an Ogive-cylinder body at high angles of attack were carried out. A parametric study was performed to investigate the influence of grid resolution and numerical scheme on the simulation. For Bounded Central scheme, the refinement in the axial direction increased the oscillations in the normal force and the magnitude of side force. On the other hand, the Central scheme produced consistent variation in normal and side force with grid refinement. The study also illustrated the development of asymmetric wake-vortex in the absence of artificial forcing or perturbations.

Acknowledgments

This work was supported by (KACST) under the NSTIP program - Project. No. (8-SPA135-3). Computations were performed on Aziz Supercomputer at KAU HPC Centre (http://hpc.kau.edu.sa/). The authors would like to acknowledge the technical support provided by the centre.

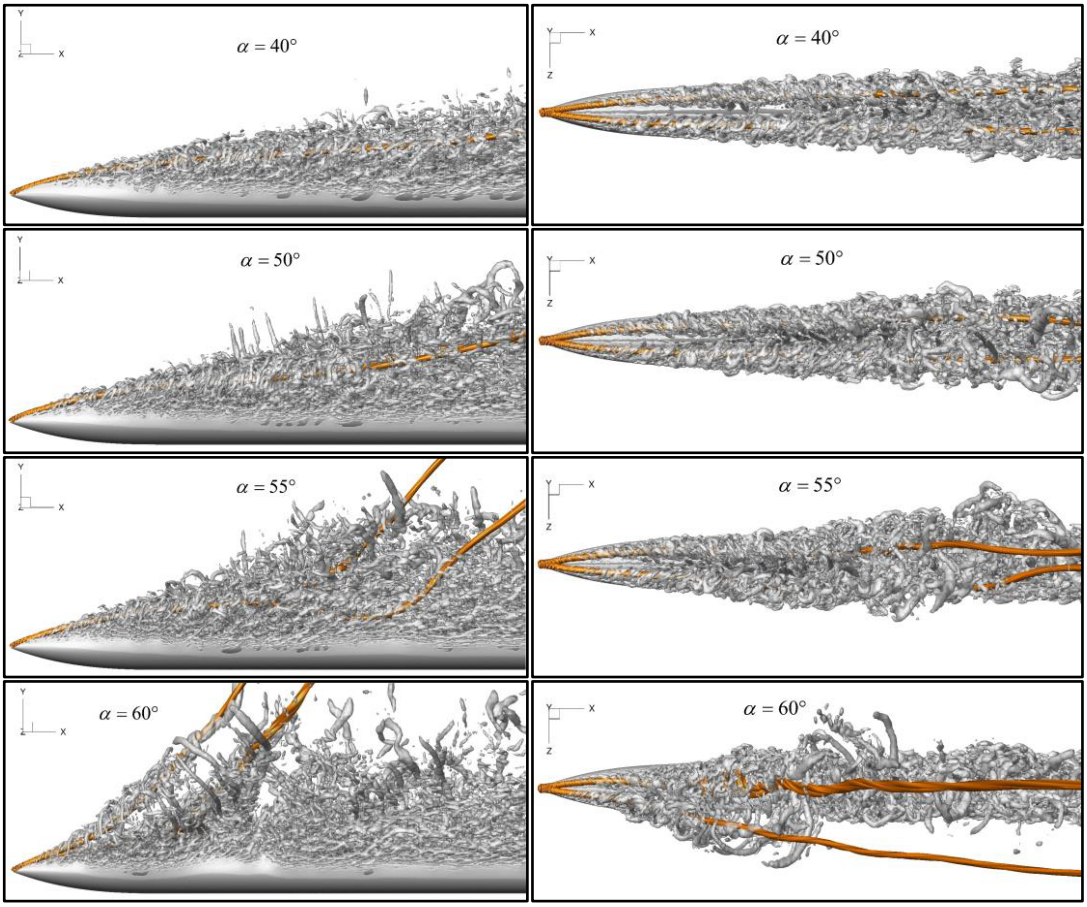

Figure 6: Instantaneous -2 isosurface and streamtubes for various angles of attack.

References

[1] D. Degani and L. Schiff, *AIAA journal,* **29**, 344 (1991)
[2] S. M. Murman, *AIAA Journal,* 2000-4103 (2000)
[3] P. Kumar and J. K. Prasad, *Journal of Spacecraft and Rockets*, **53**, 195 (2016)
[4] B. Ma, Y. Huang, and T. Liu, *Chinese Journal of Aeronautics,* **27**, 772 (2014)
[5] G. G. Zilliac, D. Degani, and M. Tobak, *AIAA journal*, **29**, 667 (1991)
[6] P. C. Dexter and B. L. Hunt, *AIAA, 19th Aerospace Sci. Mtg* (1981)
[7] E. R. Keener, G. T. Chapman, L. Cohen, and J. Taleghani, *NASA-TM-X-3437* (1977)
[8] A. B. Wardlaw and A. M. Morrison, *Journal of Spacecraft and Rockets*, **13**, 589 (1976)
[9] D. Degani and Y. Levy, *AIAA journal*, **30**, 2267 (1992)
[10] M. Germano, U. Piomelli, P. Moin, and W. H. Cabot, *Physics of Fluids A: Fluid Dynamics (1989-1993)*, **3**, 1760 (1991)
[11] D. K. Lilly, *Physics of Fluids A: Fluid Dynamics (1989-1993)*, **4**, 633 (1992)
[12] D. Degani and G. Zilliac, *AIAA journal*, **28**, 642 (1990)